

Raman lidar measurements of water vapor and cirrus clouds during the passage of Hurricane Bonnie

D. N. Whiteman,¹ K. D. Evans,² B. Demoz,² D. O'C. Starr,¹ E. W. Eloranta,¹
D. Tobin,³ W. Feltz,³ G. J. Jedlovec,⁴ S. I. Gutman,⁵ G. K. Schwemmer,¹
M. Cadirola,² S. H. Melfi,² and F. J. Schmidlin¹

Abstract. The NASA GSFC Scanning Raman Lidar (SRL) was stationed on Andros Island in the Bahamas during August–September 1998 as a part of the third Convection and Moisture Experiment (CAMEX 3) which focused on hurricane development and tracking. During the period August 21–24, Hurricane Bonnie passed near Andros Island and influenced the water vapor and cirrus cloud measurements acquired by the SRL. Two drying signatures related to the hurricane were recorded by the SRL and other sensors. Cirrus cloud optical depths (at 351 nm) were also measured during this period. Optical depth values ranged from less than 0.01 to 1.5. The influence of multiple scattering on these optical depth measurements was studied. A correction technique is presented which minimizes the influences of multiple scattering and derives information about cirrus cloud optical and physical properties. The UV/IR cirrus cloud optical depth ratio was estimated on the basis of a comparison of lidar and GOES 8 measurements. Simple radiative transfer model calculations compared with GOES satellite brightness temperatures indicate that satellite radiances are significantly affected by the presence of cirrus clouds if IR optical depths are ~ 0.005 or greater. Using the International Satellite Cloud Climatology Project (ISCCP) detection threshold for cirrus clouds on the GOES data presented here, a high bias of up to 40% was found in the GOES precipitable water retrieval.

1. Introduction

Raman lidar has long been regarded as one of the leading techniques for remotely quantifying numerous atmospheric parameters, including water vapor, aerosols, temperature, and clouds. Because of this broad measurement capability, the NASA Goddard Space Flight Center (GSFC) Scanning Raman Lidar (SRL) was selected to participate in the NASA-sponsored CAMEX-3 (third Convection and Moisture Experiment) hurricane study program which occurred during the months of August and September 1998. The SRL was stationed on Andros Island, Bahamas, during the experiment and acquired nearly daily measurements of water vapor, aerosols, and clouds. SRL measurements of the variation of water vapor and cirrus clouds during the nearby passage of Hurricane Bonnie from August 21 to 24 are presented here and constitute the first ground-based lidar water vapor and cirrus cloud measurements acquired in a hurricane environment.

Significant drying episodes during the passage of Hurricane Bonnie were observed and are likely due to midtropospheric subsidence. The influence of multiple scattering on hurricane-

induced cirrus cloud optical depth measurements was studied. A new cirrus cloud analysis technique will be presented which corrects for the influence of multiple scattering and also determines important optical and physical properties of the cirrus clouds. Cirrus cloud optical depths measured in the ultraviolet region of the spectrum are then translated to optical depths at the 11 and 12 μm channel location of the GOES satellite. Using these IR optical depth values, the influence of hurricane-induced cirrus clouds on GOES retrievals will be studied by comparing radiative transfer model simulations to retrieved surface temperatures and precipitable water. Using the International Satellite Cloud Climatology Project (ISCCP) [Rossow and Schiffer, 2000] cirrus detection threshold on GOES data, the influence of undetected cirrus on GOES measurements will be studied.

2. CAMEX 3

Errors in prediction of hurricane track and thus landfall location are dangerous for inhabited areas and can lead to unnecessary evacuation expense; and yet, small changes in initial atmospheric conditions can lead to large differences in the forecast of hurricane track and intensification [Ramamurthy and Jewitt, 1999]. Because of this, CAMEX 3 was sponsored by the NASA Atmospheric Dynamics and Remote Sensing Program with the goal of acquiring detailed atmospheric measurements which can be used to help improve hurricane model initialization and forecasting. Several instrumented aircraft were sited at Patrick Air Force Base in Florida and made numerous flights in and near Hurricanes Bonnie, Danielle, Earl, and Georges as a part of this effort. Active and passive remote sensing instruments onboard these aircraft were used

¹Earth Sciences Directorate, NASA Goddard Space Flight Center, Greenbelt, Maryland.

²University of Maryland, Baltimore County, Catonsville, Maryland.

³Space Science and Engineering Center, University of Wisconsin, Madison, Wisconsin.

⁴NASA Global Hydrology and Climate Center, Marshall Space Flight Center, Huntsville, Alabama.

⁵NOAA Forecast Systems Laboratory, Boulder, Colorado.

to measure numerous atmospheric parameters including water vapor, winds, temperature, rainfall velocities, and lightning (<http://ghrc.msfc.nasa.gov/camex3/>).

A highly instrumented ground station was established on Andros Island in the Bahamas at the U.S. Navy Atlantic Undersea Test and Evaluation Center (AUTC) as a part of CAMEX 3. Analysis of historical data indicated that the prevailing winds at AUTC are out of the southeast during hurricane season. This indicated that this land-based location on the windward coast of the island should give a good representation of the water vapor conditions over the open ocean. In addition to the SRL this site included a University of Wisconsin atmospheric emitted radiance interferometer (AERI) [Feltz *et al.*, 1998], radiosonde launches provided by both the NASA GSFC Wallops Flight Facility and the University of Wisconsin, Global Positioning System (GPS) measurements of total precipitable water, Cimel Sun photometer measurements of total precipitable water and aerosol optical depth at several wavelengths [Reid *et al.*, 1999], chilled mirror hygrometer (<http://www.humid.com/geiindex.html>) measurements of relative humidity, and standard ground measurements of temperature, pressure, and relative humidity.

The ground station served two main functions during CAMEX 3: (1) as a calibration and validation facility for CAMEX 3 and (2) as a source of highly detailed, long-term measurements of water vapor, aerosols, temperature, and other parameters in the subtropics during hurricane season. Throughout the experiment, the research aircraft made numerous calibration/validation overflights of Andros Island allowing ground-based and airborne measurements of water vapor, temperature, and winds to be compared. In this paper we will describe a short segment of the nearly 2 months of measurements acquired at the ground facility: a 4 day sequence of water vapor and cirrus cloud measurements taken between August 21 and 24, 1998, when Hurricane Bonnie was in the vicinity of Andros Island. We believe that this combined set of measurements to be the highest quality water vapor and cirrus cloud data ever acquired in a hurricane environment. The Scanning Raman Lidar and the other water vapor-measuring instruments used in this study will next be briefly described.

3. Scanning Raman Lidar

The Scanning Raman Lidar is a mobile lidar system designed to measure water vapor [Melfi *et al.*, 1989; Whiteman *et al.*, 1992], aerosols [Ferrare *et al.*, 1992, 1998], cloud liquid water [Melfi *et al.*, 1997], cloud droplet radius and number density [Whiteman and Melfi, 1999], cloud base height [Demos *et al.*, 2000], and upper tropospheric temperature [Evans *et al.*, 1997]. The SRL detects light backscattered by molecules and aerosols at the laser wavelength as well as Raman-backscattered light from water vapor (3657 cm^{-1}), nitrogen (2329 cm^{-1}), and oxygen (1555 cm^{-1}) molecules. The SRL employs two different lasers for its measurements; a XeF excimer laser (351 nm output) for optimized nighttime measurements and a tripled Nd:YAG laser (354.7 nm) for daytime measurements. The receiving telescope is a 0.76 m, F/5.2, variable field-of-view (0.25–2.5 milliradians) Dall-Kirkham system mounted horizontally on a 3.7 m optical table. The telescope field of view is steered with a large ($1.2\text{ m} \times 0.8\text{ m}$), motorized flat mirror that rotates on a horizontal axis and is also mounted on the optical table. The optical table can be slid out the back of the trailer to allow atmospheric profiles to be acquired at any angle in the

plane perpendicular to the trailer or continuously scanned from horizon to horizon. Alternatively, the lidar system may be operated completely inside the trailer by directing the output laser beam through one of three windowed openings in the trailer. Use of these windows allows vertical measurements at 5° – 10° above the horizon in either direction to be acquired. It also allows measurements to be made during rainfall. All of the SRL instrumentation, including lasers, large-aperture telescope, and data acquisition electronics, is housed within a single environmentally controlled mobile trailer that also has separate areas for new experiment development and work space for several experimenters to perform data acquisition and data analysis. More information on the lidar instrument has been published recently [Whiteman and Melfi, 1999] and is available at our website <http://virl.gsfc.nasa.gov/srl/index.htm>. The SRL measurements acquired during the passage of Bonnie were made during the nighttime to maximize the signal-to-noise ratio of the data.

3.1. SRL Water Vapor Mixing Ratio Calibration

While it is possible to calibrate a Raman lidar absolutely [Sherlock *et al.*, 1999], our past calibration efforts have demonstrated that a careful selection of radiosonde data [Ferrare *et al.*, 1995], along with the use of a nitrogen filter calibration transfer technique [Vaughan *et al.*, 1988] [Whiteman *et al.*, 1992], yields a stable lidar calibration constant. For a period of ~ 7 years, from the first field deployment of the SRL for the Spectral Radiance Experiment in Coffeyville, Kansas, in 1991 [Ellingson and Wiscombe, 1996] until the CAMEX-3 deployment in 1998, the calibration constant of the SRL determined by comparison with a selection of Vaisala radiosonde data varied only $\pm 3\%$. The calibration constant is the number by which the processed ratio of water vapor and nitrogen lidar signals must be multiplied to obtain water vapor mixing ratio [Whiteman *et al.*, 1992]. Optical modifications were made to the SRL prior to the CAMEX-3 deployment which changed the calibration constant. This fact, coupled with concerns about the calibration of the Vaisala radiosondes launched during CAMEX 3 [Miller *et al.*, 1999], necessitated a more careful examination of the SRL water vapor calibration. For the CAMEX-3 field campaign we implemented a new calibration technique [Evans *et al.*, 2000], which assumes that the atmosphere is saturated at the base of a cloud.

3.1.1. Cloud base calibration technique. Very frequently during the CAMEX-3 field campaign, small cumulus clouds developed at the top of the marine boundary layer that was present at the SRL site. The atmosphere below these clouds was typically well mixed and therefore was characterized by an approximately constant water vapor mixing ratio. These facts permitted the SRL water vapor calibration to be derived using the SRL measurements of water vapor acquired just below the cloud. The saturation mixing ratio was calculated at cloud base using temperature and pressure from a simultaneously launched radiosonde. This saturation mixing ratio was then used to derive the calibration constant to convert the ratio of lidar signals into water vapor mixing ratio [Whiteman *et al.*, 1992].

On 23 separate occasions during the CAMEX-3 experiment, the SRL water vapor measurements were calibrated in this manner. The mean calibration constant calculated from these comparisons is $\sim 12\%$ higher than the value that had been used for the previous 7 years of experimentation. This new SRL

calibration constant has been used to analyze the data presented here.

For comparison the SRL calibration constant was also determined in the traditional fashion using the Vaisala radiosondes launched during the experiment. The radiosonde measurements were first rescaled to compensate for errors due to package contamination [Miller *et al.*, 1999] [Lesht, 1999]. The mean Vaisala-derived and cloud-base-derived calibration constants agreed to much better than 1%. The standard deviation of the Vaisala-derived calibration constant was 5%, while the standard deviation of the cloud-base-derived calibration constant was 3%. Therefore during the CAMEX-3 field campaign the new cloud base calibration technique agreed well with the traditional radiosonde calibration technique and showed more consistent results.

4. CAMEX-3 Ground Site Water Vapor Instrumentation

Total precipitable water (TPW) vapor measurements from several different instruments have been analyzed as a part of this study. These instruments are the SRL, Trimble SSI GPS (University of Wisconsin (U. Wisc.)), Vaisala RS-80 radiosonde (U. Wisc.), VIZ hygistor radiosonde (WFF), Cimel Sun photometer (NASA GSFC), GOES satellite, and a combined technique that uses the AERI (U. Wisc.) and GOES. All of the ground-based instruments except the Cimel Sun photometer were located within a 100 m radius ~ 1 km from the east coast of Andros Island. The Sun photometer was located ~ 1 km west of the other instruments. The SRL measurements were limited to the nighttime periods, while the Sun photometer data were limited to daytime. The instruments use different techniques to make their measurements of TPW which can influence the values derived. The instruments and those techniques will be briefly summarized here.

4.1. Atmospheric Emitted Radiance Interferometer (AERI)

The University of Wisconsin AERI instrument [Feltz *et al.*, 1998] measures infrared radiation between ~ 3 and $20 \mu\text{m}$ with less than 1 wavenumber (cm^{-1}) resolution using a Fourier transform infrared spectrometer. Radiance spectra acquired every 10 min are transformed into vertical temperature and water vapor profiles by inverting the radiative transfer equation [Smith *et al.*, 1999]. The first-guess water vapor solution is a hybrid profile using a statistical ensemble of radiosonde measurements for the boundary layer and the National Centers for Environmental Prediction (NCEP) GOES satellite profile above the boundary layer [Turner *et al.*, 2000]. The AERI retrievals that result are limited to an altitude of ~ 3 km. To calculate TPW, the GOES water vapor profile is used above the height of the AERI retrieval [Turner *et al.*, 2000]. If coincident GOES retrievals are not available, the closest available retrieval is used. The AERI instrument that was deployed to Andros Island is similar to automated ones that have been installed at the Southern Great Plains (SGP) site of the Department of Energy (DOE) Atmospheric Radiation Measurements (ARM) Program [Turner *et al.*, 2000]. On the basis of an extensive comparison of AERI plus GOES and the microwave radiometer at the DOE SGP site, the root-mean-square (RMS) difference between the total precipitable water retrievals from the two instruments was ~ 0.8 mm [Schmit *et al.*, 2000].

4.2. Radiosondes

VIZ (manufactured by Sippican, Inc.) and Vaisala radiosondes were launched from the Andros ground site during CAMEX 3 and acquired profiles of relative humidity, temperature, pressure, and winds. The VIZ water vapor sensor is a carbon hygistor which uses changes in resistance to determine relative humidity. This is the radiosonde that was the standard for the U.S. during the latter half of the 20th century. Data processing errors in retrieving relative humidities from these radiosondes have been discussed [Wade, 1994] and new algorithms addressing these limitations implemented [Elliot *et al.*, 1998]. The Vaisala RS-80 radiosonde uses a thin polymer film whose dielectric properties change as a function of the amount of water vapor. The changes in capacitance created by these changes in dielectric constant are converted into relative humidity. Since 1998, it has been the preferred radiosonde used by the U.S. weather service. Relative humidity errors due to packaging of the radiosondes have been found [Miller *et al.*, 1999] and algorithms implemented to correct for package contamination [Lesht, 1999]. Radiosonde measurements of total precipitable water are calculated from the profile of relative humidity and have been characterized as being accurate to the 1 mm level [Wolfe and Gutman, 2000].

4.3. Cimel Sun Photometer

The Cimel Sun photometer is a solar-tracking instrument that monitors direct and diffuse solar radiation from which aerosol optical thickness, aerosol size distribution, aerosol phase function, and precipitable water vapor are retrieved [Reid *et al.*, 1999]. The Sun photometer was deployed to Andros Island as a part of NASA's AERONET (Aerosol Robotic Network) effort (<http://aeronet.gsfc.nasa.gov:8080/>). The goal of this program is primarily to measure aerosol properties. Because of this, the precipitable water vapor measurements are currently believed to have an error of approximately $\pm 10\%$ (B. Holben and T. Eck, NASA GSFC, private communication, 2000). The total precipitable water retrievals from Cimel presented here use the standard processing algorithm based on Lowtran line strengths. Recent results by Giver *et al.*, [2000], indicating errors in the Hitran-96 line strength database, would reduce the Cimel retrievals of total precipitable water by 13% [Schmid *et al.*, 2000]. Errors in line strengths such as described by Giver *et al.* are problems for all optical instruments retrieving water vapor from the 940 nm water vapor absorption band and is therefore actively being studied [Schmid *et al.*, 2000].

4.4. Global Positioning System (GPS)

The measurement of total precipitable water vapor using ground-based GPS receivers is accomplished by estimating the excess zenith-scaled signal delay caused by the neutral atmosphere [Wolfe and Gutman, 2000; Duan *et al.*, 1996]. The measurement uses observations from all GPS satellites in view at a fixed site and requires improved GPS satellite orbits and Earth orientation parameters that are supplied by any one of the International GPS Service Orbit Centers [Buetler *et al.*, 1994]. The signal delays are caused by changes in atmospheric refractivity associated with temperature, pressure, and water vapor along the paths of the signals within a radius of about 11 km of a site in the midlatitudes.

During CAMEX 3, two different software packages and improved GPS satellite orbits were used to estimate the zenith tropospheric delays from the data acquired at Andros Island.

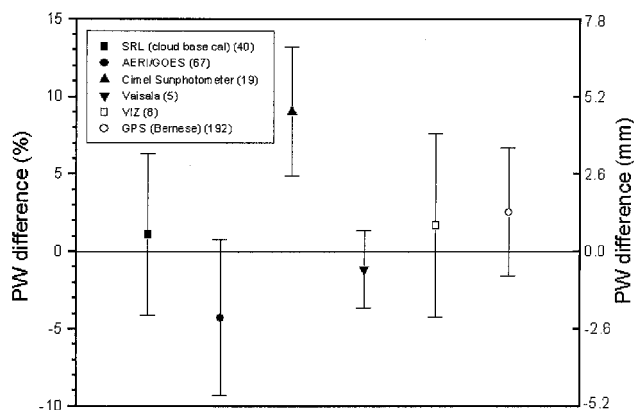


Figure 1. Precipitable water vapor differences among the various sensors stationed at Andros Island, Bahamas, during the period August 21–24 when Hurricane Bonnie passed nearby. The arbitrarily chosen baseline for the comparison is the GAMIT-processed GPS data. The error bars plotted show the standard deviation of the differences with respect to the GAMIT baseline. The number of data points for each instrument is shown in the figure legend.

One estimate was made by the NOAA Forecast Systems Laboratory (FSL) in Boulder, Colorado, using GAMIT software developed by the Massachusetts Institute of Technology and improved orbits provided by the Scripps Orbit and Permanent Array Center (SOPAC) at the Scripps Institution of Oceanography. Another estimate was made by the GPS Science and Technology (GST) program within the University Consortium for Atmospheric Research (UCAR) in Boulder, using Bernese software developed by the University of Bern and CODE Astronomical Institute orbits from the University of Bern. Using either technique, precipitable water values are determined at ~ 30 min intervals. Comparisons of GPS-derived TPW versus radiosonde have indicated mean differences of less than 1 mm with an RMS difference also of less than 1 mm [Wolfe and Gutman, 2000].

5. Comparison of TPW Measurements

The relative calibration of these instruments (or in the case of GPS, the data processing techniques) has been studied for the Bonnie passage period of August 21–24. The mean differences in TPW during this 4 day sequence of data are shown in Figure 1 where the GAMIT-processed GPS precipitable water vapor measurements were chosen as a baseline since they fell roughly in the middle of the distribution. The mean differences are calculated using the number of comparisons shown in the figure legend. The error bars indicate the standard deviation of the differences. For all sensors except the radiosonde and the Cimel, 30 min average data sets were used. The radiosonde produces profiles which take approximately 1 hour to acquire. The Cimel data frequency varied from a few minutes to more than 30 min, therefore a strict half-hour average was not always possible for the Cimel. All of the data shown later in Figure 3 were used to determine the statistics for this plot.

The Cimel Sun photometer results are the wettest of the group with a high bias of $\sim 9\%$ with respect to the GAMIT GPS. It should be noted, though, that this comparison is based just on 2 days of measurements since the instrument was dismounted during the day on August 22 as a part of hurricane

preparations at AUTEC. As discussed earlier, if the retrievals had been performed with the new line strengths according to Giver *et al.* [2000], the total precipitable water results should be 13% lower. This would change the Cimel results from a wet bias of 9% to a dry bias of 4%.

Discounting the Cimel, the water vapor instrument relative calibrations agree to within approximately $\pm 3\text{--}4\%$ or 1.5–2 mm. The SRL is $\sim 1\%$ wetter than the baseline GAMIT GPS data, while the Bernese-processed GPS data were $\sim 3\%$ wetter than the baseline. The relative difference between the two methods of GPS processing is consistent with other investigations [Revercomb *et al.*, 1998]. It is thought to come from slight differences in data processing strategies. The VIZ and Vaisala radiosondes were within 1–2% of the baseline with the VIZ showing wetter measurements than the Vaisala. The AERI plus GOES retrievals were the driest of the group with average values $\sim 4\%$ lower than the baseline. These AERI plus GOES results seem to be consistent with others, which indicated a tendency toward a dry bias as the TPW increases [Schmit *et al.*, 2000].

The spread in the relative calibration of the instruments shown in Figure 1 exceeds the claimed accuracy of many of the instruments. The results shown in the figure are an indication of the challenges inherent in accurate measurement of atmospheric precipitable water vapor. On the basis of previous studies of such differences [Revercomb *et al.*, 1998] and discounting the Cimel measurements, this level of agreement is actually quite good, however. We are aware of no other long-term water vapor measurements of this quality acquired in the subtropics during the passage of a hurricane. While the uncertainties in these water vapor measurements presented here can translate into significant errors in radiative transfer calculations [Ellingson and Wiscombe, 1996], they nonetheless represent a significant improvement over radiosondes alone for studying hurricane evolution.

6. Precipitable Water Vapor Measurements During the Passage of Hurricane Bonnie

Bonnie became a hurricane on the evening of August 22, 1998, at a point eastward of the Bahamian islands. The GOES water vapor image of Bonnie at 0615 UT is shown in Figure 2. Andros Island is indicated by the square in the middle.

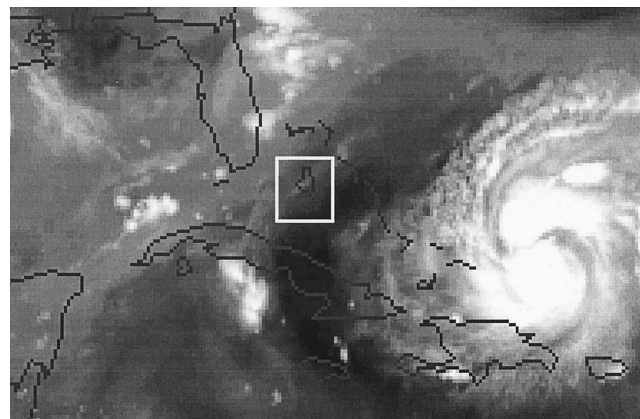


Figure 2. GOES water vapor imagery at 0615 UT on the night of August 22, 1998. Andros Island is indicated by the square in the middle. Notice the dry subsidence region to the west of the hurricane.

Over the next 4 days, Bonnie followed a generally northwest track striking the mid-Atlantic coast of the United States on the evening of August 26. The point of closest approach of the center of the hurricane to Andros Island (24.7°N , 77.8°W) was at a distance of ~ 500 km to the east northeast of Andros on the evening of August 24. Figure 3 shows TPW measurements made by the ground-site instruments during the passage of Hurricane Bonnie. As Bonnie approached Andros over the period of August 21–22, there was a distinct drying indicated by all instruments during this period. Values of precipitable water vapor changed from ~ 60 mm on August 21 to ~ 40 mm on August 22. We believe this drop in TPW to be due to compensating subsidence in the midtroposphere due to the hurricane. During August 22 and most of August 23 the TPW shows a gradual moistening to values of ~ 50 mm by midday on August 23 as the subsidence region moved to the west of Andros. Later on August 23 and into August 24, a developing wave disturbance over the gulf of Mexico blocked and reversed the westward movement of the dry region. This resulted in a secondary dry feature in the Andros TPW measurements by 0000 UT on August 24.

While the general agreement in the TPW measurements reported by the various sensors is quite good, there are interesting discrepancies to mention. The high bias in the Cimel measurements is evident. Differences among the other instruments can be explained, at least in part, by the fact that the instruments use different techniques to make their measurements of precipitable water vapor, which can influence the values derived. For example, in general, the SRL and GPS values compare reasonably well. However, the SRL data acquired on August 22 are in general lower than either of the GPS retrievals. This may be due to the volume averaging that occurs as a result of using 6–10 more-or-less randomly distributed GPS satellites to measure the zenith-scaled tropospheric signal delay. Satellite imagery tends to support this conclusion as well. The GOES-8 images, such as the one shown in Figure

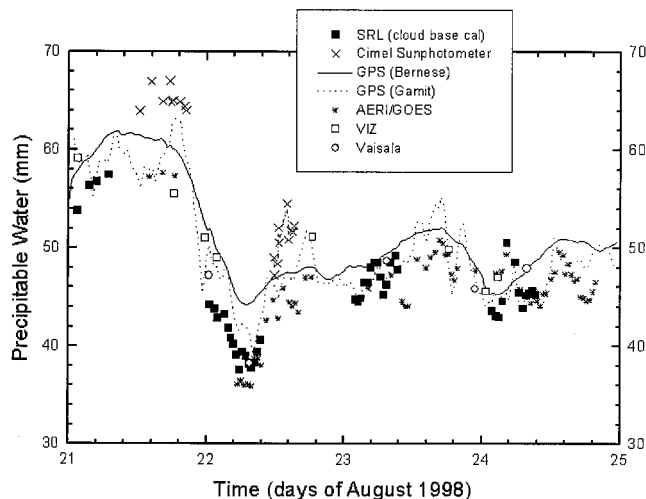


Figure 3. Evolution of precipitable water vapor as measured by Raman lidar, AERI plus GOES, GPS (with two different processing algorithms), two types of radiosonde and Sun photometer. Two drying periods associated with midtropospheric subsidence are evident: early on August 22 and 24 (UT). The sensors agree in the general trends, but there are specific differences that can be attributed to measurement techniques. See text for details.

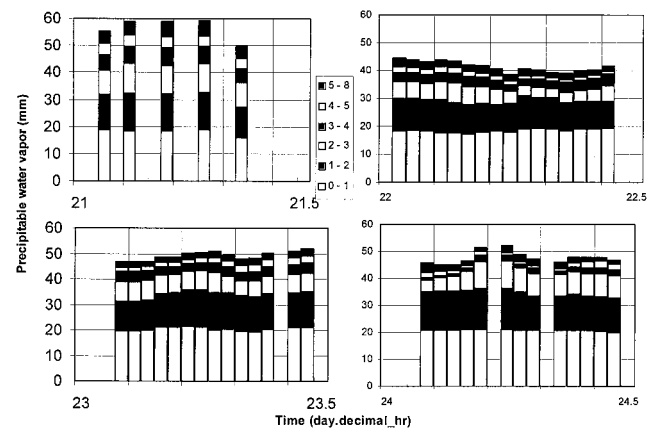


Figure 4. Precipitable water vapor measured by the lidar has been separated into the contributions due to the layers 0–1, 1–2, 2–3, 3–4, 4–5, and 5–8 km. This quantifies the change in column water vapor as a function of height. There was little change in the 0–1 km layer throughout this 4 day period indicative of a marine boundary layer. Significant changes are evident, however, in other layers.

2, indicate that for much of the night of August 22 UT, the Andros ground site was at the edge of the dry region. The SRL measurement of TPW was made directly over the ground site, while the GPS averaged over a region which included more moist air from surrounding regions.

Another example of a discrepancy between the GPS and the SRL that can be explained by the averaging volume used is seen in the data of August 24. Here a difference of up to 8 mm is seen between the SRL and the GPS TPW values. This can be explained by the presence of localized clouds and showers over the Andros ground site during the night of August 24 which greatly increased the TPW measured by the lidar but which did not significantly affect the GPS measurements.

A final interesting point to mention concerning this figure is the different structure revealed by the two GPS retrievals which are reported at approximately the same 30 min intervals. This is due to different constraints used in the retrievals that determine how much the water vapor content can change in a short period of time. The GAMIT-processed retrievals are much less constrained than the Bernese results, which allows for more structure in the GAMIT retrievals.

6.1. Water Vapor Evolution As a Function of Height

The profile measurements of water vapor made by the SRL can be used to study the height dependence of the changes in precipitable water seen in Figure 3. The SRL water vapor measurements have been divided into layers and integrated to yield the precipitable water vapor by layer. These results are shown in Figure 4. The layers used are 0–1, 1–2, 2–3, 3–4, 4–5, and 5–8 km.

In general, Figure 4 shows that the 0–1 km layer changes very little during the 4 day sequence, while precipitable water (PW) vapor contributions from the other layers vary appreciably. This indicates that most of the boundary layer moisture was under local control due to evaporation from the ocean, which is characteristic of a marine boundary layer. By contrast, middle and upper tropospheric moisture was greatly influ-

enced by the subsidence associated with hurricane Bonnie. For example, between the nights of August 21 and 22, the largest differences in precipitable water vapor occurred in the 2–3 km layer with values changing from 8–10 mm to 4–6 mm. An interesting exception to the depletion of PW at higher altitudes is seen in the 2–3 km layer on the night of August 24 at ~0400 UT when rain influenced the local water vapor environment increasing PW values from ~5 mm to ~10 mm. This indicates that a significant amount of rain probably evaporated before striking the ground. (There is actually a small enhancement to the lidar PW measurements during rainfall due to Raman scattering from liquid in the rain droplets [Demos *et al.*, 2000]. We estimate that this effect increased the precipitable water vapor values in the rainfall by ~1–2 mm.)

7. Cirrus Cloud Optical Depth Measurements

Accurate measurements of sea surface temperature and total precipitable water vapor are needed to improve hurricane track and intensification forecasting. Satellites offer the best chance of providing operational data as input to hurricane models. However, it is well known that the presence of cirrus clouds can pose problems for satellite retrievals. This is because thin cirrus clouds, while having small infrared emissivities, can be very cold. Emission from these clouds can cause significant changes in satellite radiances compared to a cloud-free scene. A comparison of Raman lidar cirrus cloud optical depth measurements with retrievals of surface temperature and total precipitable water vapor from GOES-8 will now be performed to study the influence of thin cirrus on these satellite retrievals. The same 4 day period associated with the passage of Hurricane Bonnie will be considered.

The technique for calculating cirrus cloud optical depth using Raman lidar will first be briefly described. Then the magnitude of the influence of multiple scattering on these calculations will be quantified using a retrieval technique that determines both optical and physical parameters of the cirrus clouds. The optical depth values obtained in the UV will then be translated to the IR. A simple radiative transfer model will then be used to quantify the anticipated radiance seen by GOES satellite under varying cirrus conditions. Comparisons of the predictions of this model with values derived using the split window technique [Suggs *et al.*, 1998] will then be presented. Lidar-measured TPW will also be compared with TPW retrieved from GOES data. The International Satellite Cloud Climatology Project (ISCCP) [Rossow and Schiffer, 2000] cloud-screening technique will be applied to these GOES data to study the influence of undetected cirrus on GOES TPW retrievals.

7.1. Optical Depth Assuming Single Scattering

The optical depth calculation from Raman lidar is based on the molecular nitrogen (or oxygen) signal, which shows enhanced attenuation due to the presence of a cirrus cloud. The amount of this attenuation can be converted to optical depth once the atmospheric density is known. The single-scattering equation, which yields optical depth, is obtained by integrating the equation for aerosol extinction [Ansmann *et al.*, 1992] and can be written as

$$\begin{aligned} & \int_{r_1}^{r_2} [\alpha(\lambda_L, r) + \alpha(\lambda_N, r)] dr \\ &= \ln \left(\frac{r_1^2 N_N(r_2) P(\lambda_N, r_1)}{r_2^2 N_N(r_1) P(\lambda_N, r_2)} \right) \\ & - \int_{r_1}^{r_2} [\alpha_{\text{mol}}(\lambda_L, r) + \alpha_{\text{mol}}(\lambda_N, r)] dr, \end{aligned} \quad (1)$$

where r_1 is below the cloud, r_2 is above the cloud, λ_L is the laser wavelength (351.1 nm), λ_N is the wavelength of the Raman nitrogen signal (382.4 nm), $\alpha(\lambda_x, r)$ is the cloud extinction coefficient as a function of wavelength and range, $N_N(r)$ is the number density of atmospheric nitrogen (using the full atmospheric number density is equivalent) as a function of range, $P(\lambda_N, r)$ is the lidar Raman nitrogen signal, and $\alpha_{\text{mol}}(\lambda_x, r)$ is the extinction coefficient due to molecular scattering obtained from radiosonde data. Lidar measurements in cloud-clear regions indicated that aerosols did not contribute to the optical depths measured at cirrus altitudes. Also, at these wavelengths, gaseous absorption is negligible and need not be included.

Equation (1) yields the two way optical depth, which is the fundamental quantity measured by the Raman lidar. To convert this to a one way optical depth, the wavelength scaling of cloud particle scattering must be considered. Assuming an Angstrom coefficient of $k = 0$ in the following equation,

$$\frac{\alpha(\lambda_L, r)}{\alpha(\lambda_N, r)} = \left(\frac{\lambda_N}{\lambda_L} \right)^k, \quad (2)$$

which is valid for cirrus particles that are typically very large with respect to the laser wavelength of 351 nm; the one way optical depth at 351 nm is just one half of the two way optical depth shown in (1).

However, (1) does not account for any multiple scattering that may occur in the cloud. The influence of multiple scattering is mainly due to one or more forward scattering events accompanied by a single backscatter event [Eloranta, 1998]. Multiple scattering is much more likely when large particles are encountered because of the intense forward scattering diffraction peak associated with these particles. This forward scattered component is added back into the beam and decreases the apparent attenuation of the beam. Thus the influence of multiple scattering is to decrease the optical depth measured by lidar compared to the actual value. Lidar parameters such as the telescope field of view (2 mrad (milliradians) for the SRL) and the laser divergence (1 mrad) also influence the multiple-scattering component of the signal. The influence of multiple scattering on the Raman lidar measurements of optical depth during the Hurricane Bonnie passage period of August 21–24 will now be studied.

7.2. Multiple-Scattering Calculations

As mentioned above, multiple scattering is much more likely when large particles are encountered because of the intense forward scattering diffraction peak associated with these particles. As the particle size increases, forward scattered light is confined to an increasingly narrow angular cone. This makes it more likely that a photon that is scattered forward in a first scattering event will interact with another particle (the second scattering event) and be backscattered within the field of view

of the lidar receiver. Equation (1) was formulated for single scattering only where the assumption is made that if a scattering event occurs, the photon is lost from the forward propagating laser beam. Therefore in the case of large particles, which can scatter a large number of photons in the direction of the laser beam, the use of the single-scattering equations can lead to errors in the calculated quantities.

Most of the quantities derived from Raman lidar data are based on ratios of lidar signals. In case of ratio measurements, multiple-scattering influences the numerator and denominator nearly equally and thus tends to cancel [Wandinger, 1998]. Examples of these quantities are the water vapor mixing ratio, liquid water mixing ratio, aerosol scattering ratio and the aerosol backscatter coefficient. However, optical depth is calculated using only a single lidar signal (e.g., Raman nitrogen) and, in the case of large particles, can be significantly influenced by multiple scattering.

7.2.1. Multiple-scattering equations. The influence of multiple scattering on lidar signals is related to the optical depth of the scattering medium, the size of particles that are doing the scattering, the range to the scattering volume, and specific parameters of the lidar system in use. This can be seen in the formulation of the multiple-scattering equations developed by Eloranta using a Gaussian approximation for the forward scattered diffraction peak [Eloranta, 1998]. The ratio of double and triple scattering to single scattering can be expressed as

$$\frac{P_2(R)}{P_1(R)} = \frac{\mathcal{P}_2(\pi, R)}{\mathcal{P}_1(\pi, R)} \left[1 - \exp \left(-\frac{\rho_i^2}{\rho_l^2} \right) \right]^{-1} \cdot \left\{ \tau - \int_0^d \beta_s(x_1) \exp \left(-\frac{\rho_i^2 R^2}{(d-x_1)^2 \Theta_s^2(x_1) + \rho_l^2 R^2} \right) dx_1 \right\} \quad (3)$$

$$\frac{P_3(R)}{P_1(R)} = \frac{\mathcal{P}_3(\pi, R)}{\mathcal{P}_1(\pi, R)} \left[1 - \exp \left(-\frac{\rho_i^2}{\rho_l^2} \right) \right]^{-1} \cdot \left\{ \tau - \int_0^d \beta_s(x_1) \cdot \int_{x_1}^d \left[\beta_s(x_2) \exp \left(-\frac{\rho_i^2 R^2}{\left[\frac{(d-x_1)^2 \Theta_s^2(x_1) + (d-x_2)^2 \Theta_s^2(x_2) + \rho_l^2 R^2}{\rho_l^2 R^2} \right]} \right) dx_2 \right] dx_1 \right\}, \quad (4)$$

where

$$\tau = \int_0^d \beta_s(x) dx \quad (5)$$

is the optical depth. In these equations, P_n is the signal intensity due to n th-order scattering, $\mathcal{P}_n(\pi, R)/\mathcal{P}_1(\pi, R)$ is the ratio of phase functions in the backscatter direction for an n th-order-scattered photon and a singly scattered photon. For Raman backscatter this ratio is equal to 1.0 due to the broad nature of the molecular phase function near the backscatter direction. The telescope half-angle field of view is ρ_l , ρ_l is the

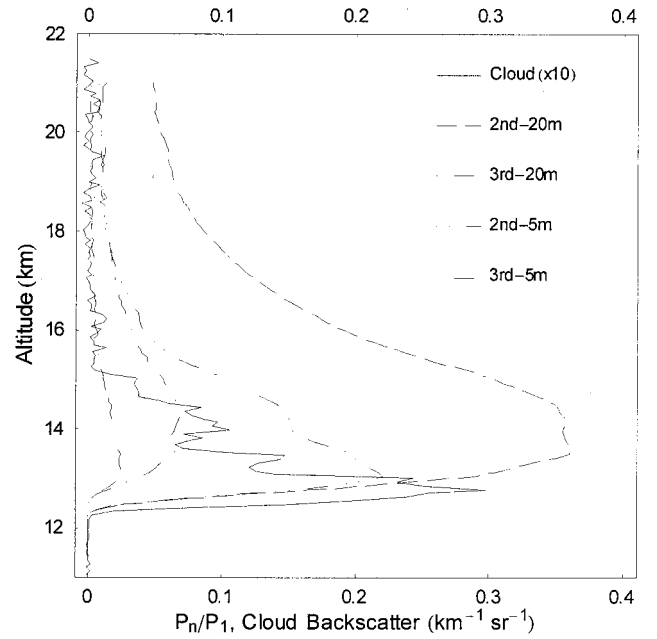


Figure 5. Multiple-scattering calculations for a cirrus cloud measured on the night of August 23, 1998. Cirrus particles of 5 and 20 μm were simulated. An extinction to backscatter ratio of 20 was used. The ratio of n th-order scattering to first-order scattering is plotted along with the cloud backscatter coefficient. The backscatter coefficient has been multiplied by 10 for easier viewing.

laser half angle divergence, d is the depth of penetration into the cloud determined by the location of the backscattering event, β_s is the extinction coefficient, and Θ_s is the $1/e$ diffraction peak angular half width. These equations have been reformulated from the published versions [Eloranta, 1998] in a manner that allows for more efficient numerical calculation. The diffraction peak angular width for spheres can be calculated from the form of the scattering amplitude for a spherical aperture calculated from diffraction theory given by [Bohren and Huffman, 1983]

$$S(\theta) = x^2 \frac{1 + \cos(\theta)}{2} \frac{J_1(x \sin \theta)}{x \sin \theta}. \quad (6)$$

Here θ is the scattering angle measured with respect to the forward direction, x is the size parameter of the spherical particle defined as the circumference divided by the radius, and J_1 is the first Bessel function of the first kind. The intensity of scattering versus angle is therefore given by

$$I(\theta) = |S(\theta)|^2. \quad (7)$$

7.2.2. Cirrus cloud multiple-scattering corrections. Cirrus clouds were above the SRL site on Andros Island for much of the night on August 23, 1998. They were characterized by quite cold temperatures ranging from -45°C to -75°C based on radiosonde measurements. A thick portion of the cirrus cloud was used to study the influence of multiple scattering on Raman lidar measurements of cirrus optical depth. The results are shown in Figure 5. In this portion of the cirrus cloud the measured optical depth (before correction for multiple scattering) was ~ 0.6 . Both second- and third-order multiple scattering were calculated assuming constant particle radii of 5 and 20 μm . These particle dimensions were chosen on the basis of

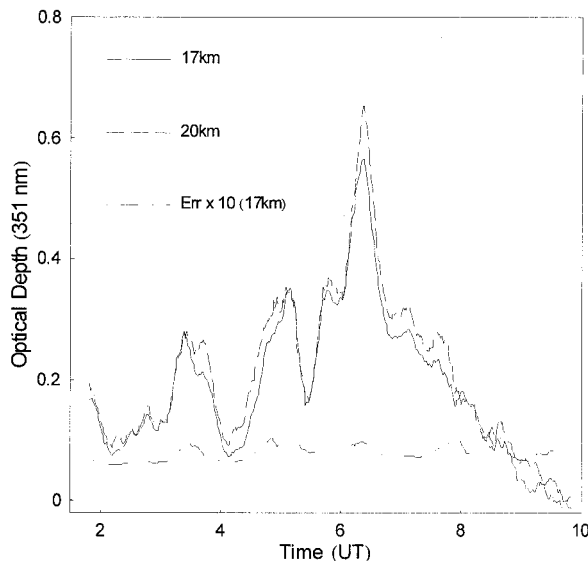


Figure 6. Optical depth calculations for a cirrus cloud measured on the night of August 23, 1998. Upper reference altitudes (r_2) of 17 and 20 km have been used to demonstrate the influence of multiple scattering. As r_2 is increased, there is a general trend toward higher optical depths as expected. The error in the optical depth retrieval ($\times 10$) is also plotted.

the retrieved particle sizes that will be presented later. For these calculations the cirrus optical depth was obtained from the lidar-derived cirrus backscatter coefficient, which is essentially uninfluenced by multiple scattering [Wandinger, 1998], using the following equation:

$$\tau = \bar{S} \int_{r_1}^{r_2} \beta(x) dx. \quad (8)$$

In (8), \bar{S} is the “bulk” extinction/backscatter ratio between r_1 and r_2 in units of sr and $\beta(x)$ is the cloud backscatter coefficient ($\text{km}^{-1} \text{sr}^{-1}$). In this context the term “bulk” is used to refer to a mean value through a cloud layer. The results shown in Figure 5 use a value of 20 for \bar{S} .

Cirrus cloud optical depth calculated using (1) requires two reference altitudes, r_1 and r_2 . The first altitude, r_1 , must be below the cloud and the second, r_2 , must be above it. One of the interesting points to make about Figure 5 is that the influence of multiple scattering on measurements of cirrus optical depth becomes smaller as the upper reference altitude is increased. This effect will be used here to correct measurements of optical depth for the influence of multiple scattering and to determine additional parameters of the cirrus cloud such as bulk extinction to backscatter ratio and bulk particle radius.

The influence of changes in the upper reference altitude on calculations of cirrus optical depth is demonstrated in Figure 6 using data acquired during the night of August 23, 1998, at Andros Island, Bahamas. Upper reference altitudes of 17 and 20 km have been used. The optical depth using $r_2 = 20$ km clearly indicates higher values, which is consistent with a multiple-scattering influence. Also plotted is the optical depth error ($\times 10$) for the 17 km calculation. The error in the optical depth calculation helps to explain why the optical depth calculations at 20 km sometimes are less than those at 17 km.

The difference in optical depth calculated at 20 and 17 km is shown in Figure 7. In general the results using $r_2 = 20$ km are

higher than for $r_2 = 17$ km with the differences as large as 0.09. However, at times around 3.0, 5.0, 8.0, and 10.0 UT, the 17 km extraction produces lower results. Nonetheless, these measurements on average provide a quantification of the multiple-scattering influence that can be used to determine other cloud parameters.

7.2.3. Cirrus cloud retrievals. The optical depth that is required in the multiple-scattering calculations using (3) and (4) is determined through the use of (8). An iterative technique has been developed to determine the correct \bar{S} that uses the optical depth difference shown in Figure 7, equations (3) and (4), and an initial value of \bar{S} that is determined by using the optical depth calculated with an upper reference altitude of 20 km. Each iteration computes a new value of \bar{S} by correcting for the multiple scattering computed using the previous value of \bar{S} . The algorithm converges very quickly since the original optical depth measurements (using $r_2 = 20$ km) are in error by typically less than 5% for these cirrus cloud measurements. The second iteration of the algorithm produces less than a 1% change in the value of the optical depth of the cloud and thus retrievals presented here use two iterations. The width of the forward scattered component of the multiply scattered light is also solved for in this technique. This is given by Θ_s , the $1/e$ half width of the forward diffraction peak, in (3) and (4). With this value known, the radius of the sphere that possesses the same diffraction properties can be determined using (6). The results of this retrieval technique are shown in Figure 8.

The original uncorrected optical depths measured at 17 and 20 km are shown in solid and dashed lines, respectively. These are the same data as in Figure 6. The corrected optical depth resulting from the iterative technique is also shown. All three of these have been multiplied by 100 for display purposes. The retrieved values for bulk extinction/backscatter ratio have a mean value in this cloud of ~ 20 . The bulk radius of the particle that has the same diffraction width as observed in the cloud is also plotted and has a mean value of $\sim 10 \mu\text{m}$.

There are several important points to make using this figure.

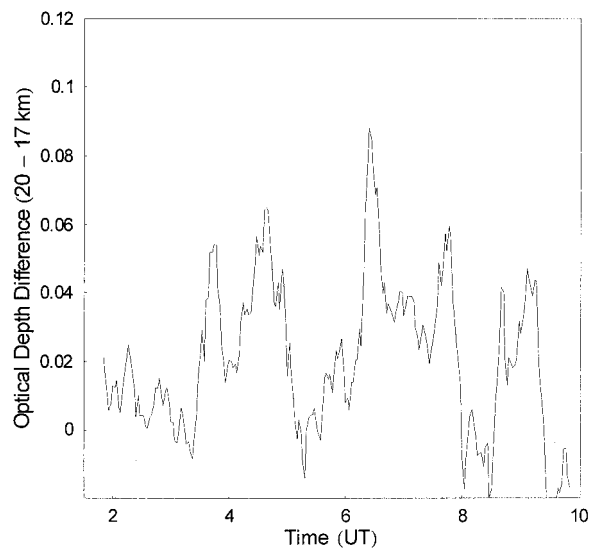


Figure 7. Optical depth difference using a 20 km upper reference altitude versus 17 km. In general, the 20 km calculations yield a higher optical depth which is consistent with multiple scattering, however the random error in the data can, on occasion, cause the 17 km value to exceed the 20 km value.

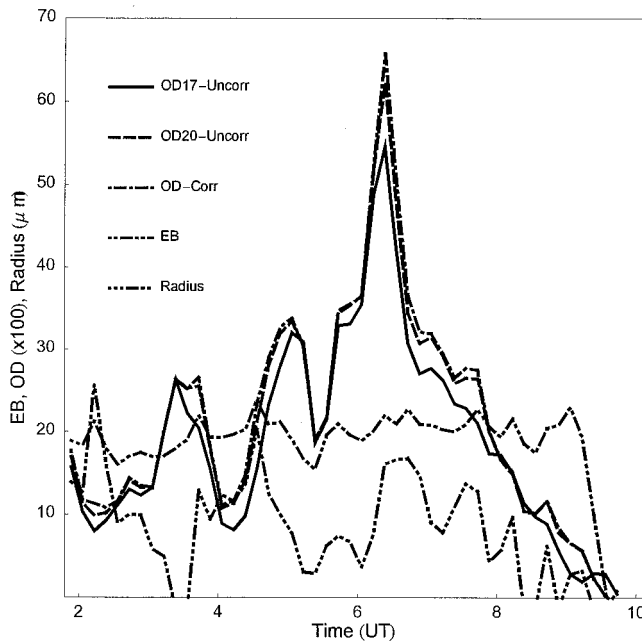


Figure 8. Results of an iterative technique are shown. This technique uses the optical depths calculated at different altitudes and the lidar-derived cloud backscatter coefficient to simultaneously correct for the influence of multiple scattering on cloud optical depth as well as to determine the bulk extinction/backscatter ratio and the radius of the sphere with the same bulk diffraction properties as measured in the cloud. The uncorrected optical depth calculations performed with $r_2 = 17$ km (solid line) and 20 km (dashed) shown in Figure 6 are repeated here. The retrieved values of corrected optical depth, bulk extinction to backscatter ratio, and particle radius are also plotted.

The first is that this technique demonstrates that Raman lidar measurements of cirrus cloud optical depth can be corrected for the influence of multiple scattering and that for these cirrus clouds this correction is small when compared to the optical depth calculated at 20 km. The average correction to the 20 km optical depth is less than 5%. A second point is that the bulk extinction/backscatter ratio of the cirrus cloud can be determined. The average value of ~ 20 for this cirrus cloud is consistent with other lidar measurements that have been made using a technique similar to this [Eloranta, 2000] [Eloranta and Piironen, 1996]. It is interesting to note that ray-tracing calculations based on actual in situ cirrus crystal measurements indicate a much broader range of extinction/backscatter ratios than has been measured by lidar [Yang et al., 1998] [Eloranta, 2000]. The reason for this is that the lidar is sensitive to the light-scattering properties of the crystals, which are related more to the particle area than to the particle long dimension. The optical theorem can be used to clarify this.

The optical theorem can be formulated as [Jackson, 1975]

$$\sigma_t = \frac{4\pi}{k} \text{Im}[\epsilon_0^* \cdot \mathbf{f}(\mathbf{k} = \mathbf{k}_0)], \quad (9)$$

where σ_t is the total cross section, including scattering and absorption, ϵ_0^* is the polarization state of the incoming photon, \mathbf{k} is the scattered wave vector, \mathbf{k}_0 is the wave vector scattered in the forward direction, and \mathbf{f} is the normalized amplitude of the scattered electromagnetic field.

It is clear from (9) that the amplitude of the forward scattered diffraction peak is directly related to the total extinction of the particle. In fact, Babinet's principle [Jackson, 1975; Bohren and Huffman, 1983], which is appropriate for large absorbing particles, implies that an equal amount of incident energy is diffracted by the particle as is absorbed by the particle. This means that the total extinction cross section of such a particle is twice the geometrical area of the particle. This result agrees with Mie theory in the large-particle limit. Therefore the forward scattered diffraction peak of the multiply scattered radiation, which determines the multiple-scattering influence on the data and forms the basis of this particle size retrieval technique, is directly related to the cross-sectional area of the particle doing the scattering.

It should be noted that the cross sectional area of a "large" ice crystal can actually be quite small because one of the crystal axes will typically be very small. In the case, then, of randomly oriented crystals the projected area of the crystals can be representative of particles much smaller than the long crystal dimension alone would imply. Other recent investigations have indicated that small dimensions may offer good representations of certain cirrus crystal properties. Grenfell and Warren [1999] have shown that calculations of cirrus multiple scattering can be estimated accurately by using a collection of equal-radius spheres to represent each cirrus crystal. The radius is chosen such that the ratio of volume to area (V/A) of the collection of spheres is equal to that of the crystal. The radius of the equal V/A sphere in the case of hexagonal columns is approximately equal to the radius of the short axis of the crystal. Thus it is sensible that typical retrieved radii, using the multiple-scattering technique described here, should roughly correspond to the dimensions of the short crystal axis. In light of these considerations and the fact that small crystals are associated with cold cirrus clouds [Yang et al., 1997; Smith et al., 1998] such as these, the small radii retrieved here seem reasonable.

7.3. Hurricane Bonnie Cirrus Clouds

Raman lidar measurements of cirrus cloud optical depth (at 351 nm) acquired at the Andros Island ground site for the nights of August 21–24 are presented in Figure 9. For the purposes of this figure, the values have been determined using 20 km as the upper reference altitude. On the basis of the analysis presented above, this approach reduces the influence of multiple scattering to a few percent at most. If higher accuracy results were desired, the full multiple scattering correction technique could be applied. A 10-min running average of lidar data has been used for these calculations. The error bars plotted indicate the uncertainty of the measurement according to Poisson statistics.

The lidar data were also used to calculate cirrus altitude and geometrical thickness. These measurements indicate cirrus cloud base height ranged from a minimum of approximately 9 km at 0530 UT on August 21 when the cloud thickness was ~ 5 km (optical depth ~ 1.5) to ~ 16 km at 0900 UT on August 24 when the thickness was less than 1 km (optical depth less than ~ 0.01). There were times when lidar optical depth measurements were not possible. These were due to rain (after 0600 on August 21), system filter changes (0200–0245 on August 21 and 0200–0330 on August 22), and low clouds (0500–0600 on August 24). The other period of no data occurs after 0600 UT on August 22 and indicates that no cirrus clouds were detected by the lidar during this time.

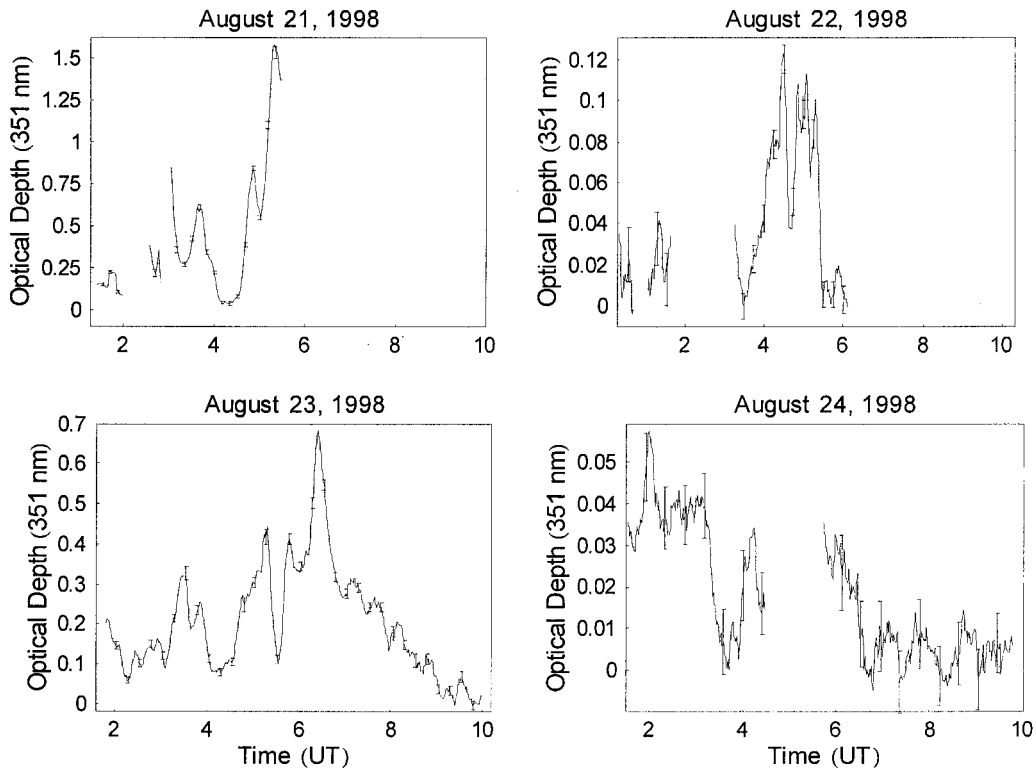


Figure 9. Four night sequences of cirrus optical depth as measured by the Scanning Raman Lidar. Values reported are for 351 nm and have been calculated using 20 km as the upper reference altitude to minimize the influence of multiple scattering. The error bars reported are those calculated from Poisson statistics based on the strength of the lidar signal. Note that the optical depth scale changes for each of the plots.

Because of the range of optical depths covered, the measurements of August 23 provided a convenient data set to test the sensitivity of satellite retrievals to the presence of cirrus clouds. On this night the measured optical depth at 351 nm

ranged from a minimum of less than 0.01 to a maximum of ~ 0.7 . (It is interesting to note that the optical depth limit (at 694 nm) for visual detection of cirrus during the daytime has been determined to be ≈ 0.03 [Sassen and Cho, 1992]). The

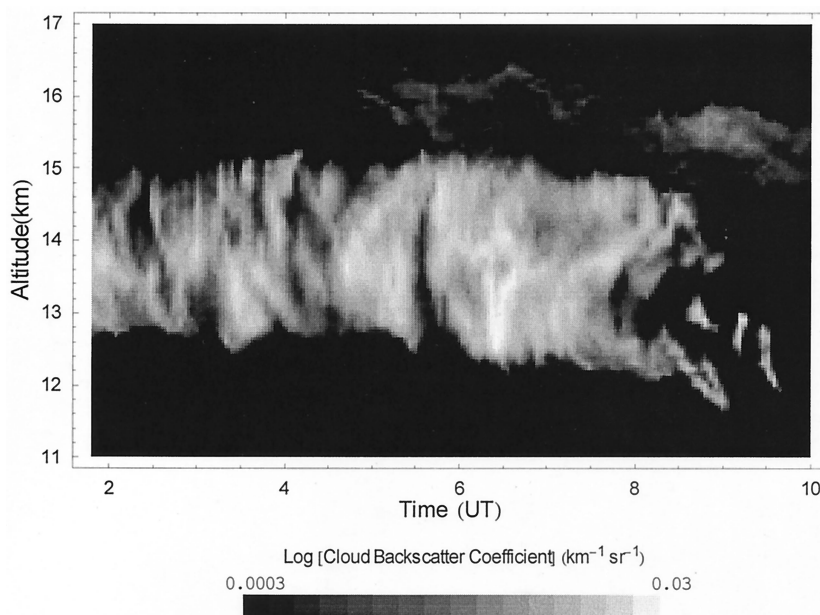


Figure 10. SRL measurements of cirrus cloud backscatter coefficient on the night of August 23, 1998, at Andros Island. This image uses vertical pointing data only.

lidar cloud backscatter coefficient image is shown in Figure 10. Here the backscatter coefficient is shown using a log scale with values ranging between $\sim 3 \times 10^{-4}$ and 3×10^{-2} ($\text{km}^{-1} \text{sr}^{-1}$).

7.3.1. Discussion of the radiative impact of cirrus clouds.

To estimate the radiative effects of these cirrus clouds, a simple radiative transfer model, which accounts for surface emissivity, surface temperature, cloud emissivity, and cloud temperature, was used. The model equation is

$$R_{\text{sat}} = (1 - \varepsilon_c) \varepsilon_s B(\lambda_{\text{sat}}, T_s) + \varepsilon_c B(\lambda_{\text{sat}}, \bar{T}_c), \quad (10)$$

where R_{sat} is the predicted satellite radiance ($\text{W m}^{-2} \text{sr}^{-1} \mu\text{m}^{-1}$), ε_c is the cirrus cloud emissivity calculated from $\varepsilon_c = (1 - e^{-\tau_c})$, where τ_c is the cirrus infrared optical depth, ε_s is the surface emissivity, $B(\lambda, T)$ is the Planck function, λ_{sat} is the wavelength of the satellite instrument channel, T_s is the surface radiating temperature, and \bar{T}_c is the mean cirrus cloud radiating temperature. The first term in (10) is the surface contribution to the satellite radiance and the second term is the contribution due to the cirrus cloud. The satellite-effective brightness temperature T_{sat} is then obtained numerically from the Planck function for the value of R_{sat} . Averaging over the GOES 11 and GOES 12 micron channel filter widths is required since the index of refraction of ice varies significantly in this region of the spectrum [Warren, 1984].

The purpose of this equation is not to yield highly accurate values of satellite radiance but rather to study the influence of varying cirrus optical depths on those radiances. Thus the radiative contribution due to atmospheric TPW, which was roughly constant during the measurement period, was not included. For the model calculations of radiance using (10), the values used were $\varepsilon_s = 0.98$, $T_s = 302$ K obtained from GOES during a cloud-clear period, $\bar{T}_c = 214$ K obtained from radiosonde measurement.

To use the lidar measured optical depths for infrared radiative transfer calculations, the optical depths must be translated to the IR. In previous studies the ratio of visible (532 nm from a Nd:YAG laser) to infrared cirrus optical depth varied between ~ 1.6 and 2.4 [Wylie *et al.*, 1995] [DeSlover *et al.*, 1999]. This is an important ratio to quantify since it translates approximately into the shortwave/longwave forcing due to a cirrus cloud. The ratio depends on particle size and, because of the changing values of the index of refraction of ice, the exact spectral locations that are being compared. These studies have indicated that the values for $11 \mu\text{m}$ can be larger than for $12 \mu\text{m}$.

To study the ratio of UV/IR cirrus optical depths, the same approach described by Wylie *et al.* [1995] was used where the cirrus IR optical depth τ_c can be approximated using the following equations:

$$\begin{aligned} \tau_c &= -\ln(1 - \varepsilon_c) \\ \varepsilon_c &= \frac{R_{\text{sat}} - \varepsilon_s B(\lambda_{\text{sat}}, T_s)}{B(\lambda_{\text{sat}}, \bar{T}_c) - \varepsilon_s B(\lambda_{\text{sat}}, T_s)}. \end{aligned} \quad (11)$$

In these equations, T_s is the surface blackbody brightness temperature determined from a clear GOES pixel. The GOES viewing angle of 29° must also be accounted for in the determination of optical depth. Using the GOES brightness temperatures during the night of August 23, which are shown later in Figure 12, the ratio of UV (at 351 nm from the SRL) and IR (at the GOES 11 and $12 \mu\text{m}$ channel positions) cirrus cloud optical depth was evaluated using (11) and is shown in Figure 11.

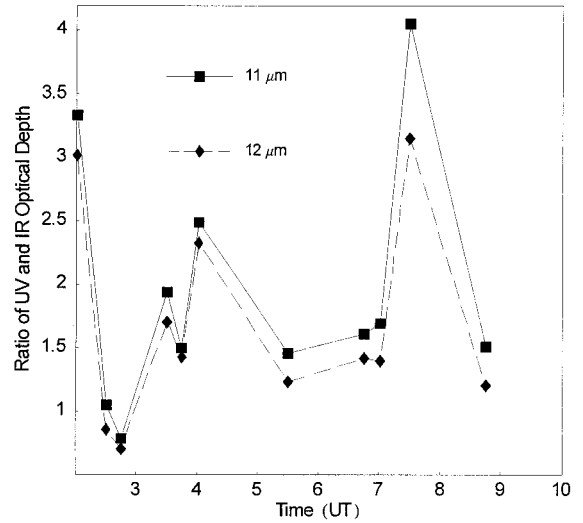


Figure 11. UV/IR cirrus cloud optical depth ratio. The ratio of optical depth at the laser wavelength of 351 nm and the GOES 11 and $12 \mu\text{m}$ channel positions determined using the technique of Wylie *et al.* [1995].

The mean values for the ratio of optical depths shown in Figure 11 are 2.2 ± 0.8 at $11 \mu\text{m}$ and 2.0 ± 0.6 at $12 \mu\text{m}$. While there is significant uncertainty in these values due to the small sample size, these results point to the conclusions that (1) the $11 \mu\text{m}$ ratio is larger than the $12 \mu\text{m}$ ratio, which is consistent with the VIS/IR ratio studies mentioned earlier [Wylie *et al.*, 1995; DeSlover *et al.*, 1999] and (2) these UV/IR values are within the range found in these same studies. It is interesting to consider these results in light of the size of the ice particles in the cloud.

Depending on the size of the crystal, ice particle extinction efficiency can change quite significantly between 11 and $12 \mu\text{m}$ due to the large changes in index of refraction of ice in this spectral region [Yang *et al.*, 1997; Smith *et al.*, 1998]. When small ice crystals are involved ($\sim 10 \mu\text{m}$ in radius), the extinction efficiency at $12 \mu\text{m}$ is significantly larger than at $11 \mu\text{m}$. This effect has been observed in thin cirrus clouds using Nimbus 4 [Prabhakara *et al.*, 1988] and airborne measurements [Smith *et al.*, 1998]. Therefore the results of Figure 11, which show an $11 \mu\text{m}$ UV/IR optical depth ratio that is larger than the $12 \mu\text{m}$ ratio, can be an indication of small particle sizes in these cold clouds (-45°C to -75°C). For very large diameter crystals such as would be expected in cirrus uncinus, the extinction efficiencies at 11 and $12 \mu\text{m}$ should be quite similar, so one would expect the two curves in Figure 11 to overlay each other [Smith *et al.*, 1998]. It should be mentioned, however, that since smaller crystals are expected at the tops of the clouds, the conclusion of small ice crystals based on the IR data alone could be influenced by a top-of-cloud bias in the IR radiances. Because of this possible bias, the location of the instrument making the IR measurement of optical depth, whether on the ground [DeSlover *et al.*, 1999], from aircraft [Smith *et al.*, 1998] or from satellite [Wylie *et al.*, 1995] must be considered in the analysis. With this in mind, the difference between the UV/IR optical depth ratios determined here and the VIS/IR optical depth ratios determined before [DeSlover *et al.*, 1999] [Wylie *et al.*, 1995] are probably related to both the particle sizes in the cirrus clouds that were studied and the techniques used to derive the IR optical depths. We will study

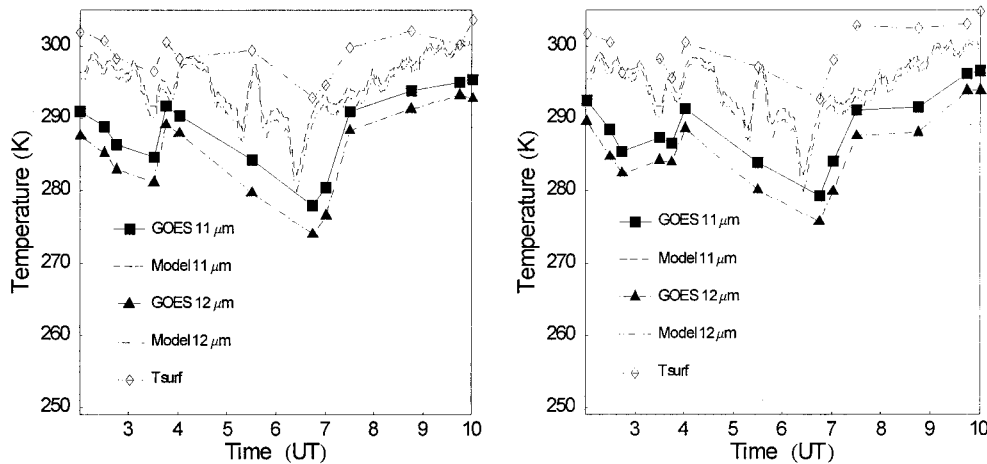


Figure 12. Comparison of GOES 11 and 12 μm channel brightness temperatures and model calculations for the satellite pixel directly over the lidar site (left) and the pixel ~ 5 km to the east of the site (right). Also plotted are the retrieved skin surface temperatures using the split-window technique. The model assumes constant surface and cloud temperatures. The two pixels show generally good correlation of features. It is evident that even very thin cirrus clouds influence satellite radiances. For comparison the cirrus optical depth values are in the next figure.

this ratio with more GOES comparisons in the future, but for this study, we have used the values of 2.2 and 2.0 as the scaling factors to adjust the lidar-measured optical depths to those appropriate for the GOES 11 and 12 μm channel positions.

Figure 12 shows the brightness temperatures calculated from (10) and the Planck function using the parameters described above for both the 11 and the 12 μm GOES channels (long dashed and dot-dot-dashed lines, respectively). Also plotted are the actual GOES 11 and 12 μm channel brightness temperatures (squares and triangles). The slight high bias of the model results with respect to the GOES data is consistent with the atmospheric contribution that was excluded from the model. The retrieved skin surface temperature using the split-window physical retrieval technique [Suggs *et al.*, 1998] are shown using diamonds. No cloud screening was performed in these retrievals. Therefore the GOES brightness temperatures and the subsequent retrievals have the effects of cloud-contamination implicitly in them. This was done for the GOES pixel that contains the lidar location (on the left-hand side in

the figure) and for the adjacent pixel ~ 5 km to the east of this location (on the right) and thus completely over the ocean. (The cirrus optical depth is plotted for comparison in Figure 13).

There are several points that can be made from this figure. Despite the sampling issues relating to the comparison of 10 min averages of lidar data and ~ 5 km satellite pixels, these simple model calculations capture the main features observed in the satellite brightness temperatures. Also, the pixels over land (left) and over water (right) show good general agreement, indicating that the constant surface temperature assumption in the model retrievals is reasonable. This being the case, the third point is that for both of these pixels, the changing cirrus cloud optical depth is the dominant factor causing fluctuations in the satellite brightness temperatures. This influence lasts until ~ 1000 UT, as indicated by the general slope in the model predictions toward higher brightness temperatures. Taking 1000 UT as an estimate of the first time during the measurement period when the satellite brightness temper-

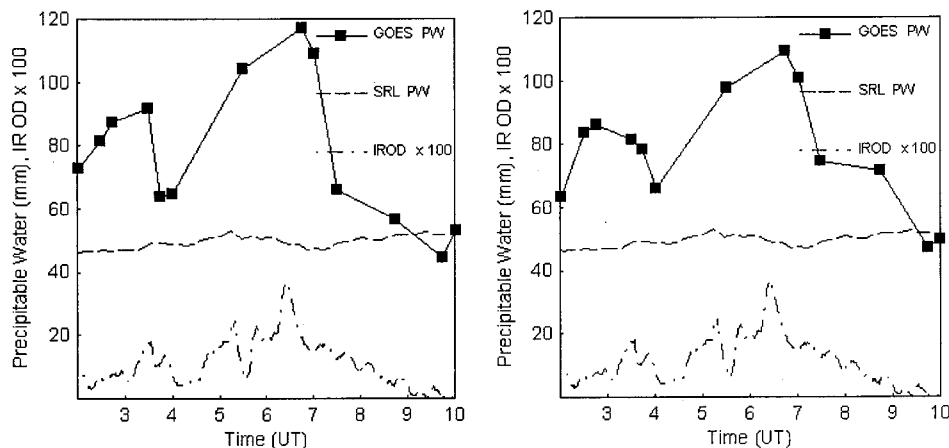


Figure 13. Retrieved total precipitable water from GOES for the satellite pixel directly over the lidar site (left) and the pixel 5 km to the east of the site. Also plotted are the SRL measurements of total precipitable water and cirrus optical depth. The correlation between satellite-retrieved PW and cirrus optical depth is clear.

atures were uninfluenced by the presence of cirrus, the IR optical depth threshold above which the presence of cirrus significantly influences GOES satellite brightness temperatures is estimated to be ~ 0.005 – 0.01 based on the IR-scaled lidar measurements. This value is approximately an order of magnitude lower than the cirrus optical depth detection threshold goal established within the EOS science plan [King, 1999] in the discussion of required satellite measurements. Thus it seems apparent that the next generation of Earth-sensing instruments may have biases in their retrievals due to undetected cirrus. It is again interesting to note the ~ 0.03 optical depth limit (at 694 nm) for visual detection [Sassen and Cho, 1992]. Using an approximate scaling factor of 2.0 [Wylie and Menzel, 1999], the IR optical depth limit for daytime visual cirrus cloud detection becomes ~ 0.015 . These results tend to indicate that even a cirrus cloud that cannot be seen by the naked eye can still have a noticeable radiative impact on satellite measurements.

The corresponding precipitable water retrievals using the split-window technique are shown in Figure 13. In this figure the lidar-derived precipitable water and the cirrus optical depth measurements (adjusted to the IR) are also plotted. The lidar measurements indicate that the TPW changed relatively little during the measurement period. All significant variation in the retrieved TPW from GOES is attributed to the influence of cirrus.

It is clear from Figure 13 that the cirrus-induced errors in the retrieval of TPW are larger than and in opposite direction to those in skin temperature shown in Figure 12. Increases in cirrus optical depth depress the retrieved surface temperature and elevate the retrieved TPW. A simple explanation for this effect can be obtained by considering the adjustments in the derived values of surface temperature or precipitable water required to account for the change in radiance due to the presence of cirrus. Because of the T^4 dependence of blackbody radiant energy, small reductions in retrieved surface temperature can explain the reduced brightness temperatures of a cirrus cloud-contaminated scene. However, large increases in precipitable water are required to bring about comparable reductions in brightness temperatures since variations in precipitable water contribute mainly to changes in emissivity of the moist atmosphere and not its temperature.

It is interesting to compare these results with other cloud studies. In their study of VAS data, Wylie and Menzel [1989] concluded that 50% of the clouds with IR optical depths of 0.1 or less went undetected. In a more recent study, based on HIRS data [Wylie and Menzel, 1999], these same authors comment that the CO_2 slicing technique used on HIRS data allows the detection of cirrus for IR optical depths above ~ 0.05 .

In the most recent ISCCP cloud data products [Rossow and Schiffer, 2000], cirrus detection was performed using a simple threshold technique based on brightness temperature. A cirrus cloud is indicated over land if the $11\text{ }\mu\text{m}$ brightness temperature is 4 K less than what is determined to be the cloud-clear value, while over water this threshold is 2 K (D. Wylie, private communication, 2000).

Using the ISCCP detection threshold over water of 2 K with the GOES brightness temperature data presented in Figure 12 yields the following results. The 2 K threshold corresponds to a cirrus cloud IR optical depth of ~ 0.05 in good agreement with the threshold determined from HIRS data. Referring to Figure 13, the GOES TPW retrieval (using the right-hand pixel over the ocean) is $\sim 20\%$ larger than the SRL value for optical

depths of 0.05. Over land, where the ISCCP cirrus detection threshold is 4 K, the cirrus optical depth threshold and the error in TWP become ~ 0.1 and 40%, respectively. This high bias is consistent with other investigations [Wolfe and Gutman, 2000]. If this example is representative of the current state of cloud detection algorithms, it seems evident that the probability that undetected cirrus are introducing a high bias into the precipitable water database derived from IR satellite measurements is high. This high bias needs to be considered in the context of hurricane model predictions since this study indicates that thin cirrus clouds are commonly found in the hurricane environment.

8. Summary and Conclusions

The NASA GSFC Scanning Raman Lidar (SRL) was stationed at Andros Island, Bahamas, during August–September 1998 as a part of the third Convection and Moisture Experiment (CAMEX 3) hurricane study program. Lidar measurements of water vapor and cirrus clouds have been compared with various other sensors during the 4 day period of August 21–24 when Hurricane Bonnie passed near the island. The relative total precipitable water calibration of the instruments was compared where the SRL measurements were calibrated, using a new cloud base calibration technique. The cloud base calibration value agrees very well with the calibration value derived from radiosonde but shows less random variation. The Cimel Sun photometer was found to exhibit a wet bias of $\sim 9\%$ compared with the baseline measurement of precipitable water from the GPS using GAMIT processing. The general agreement of the TPW measurements of the other instruments was ± 3 – 4% . Differences between the GAMIT and the Bernese processing of $\sim 3\%$ (with the Bernese technique producing wetter results) are attributed to minor differences in data processing strategies.

The evolution of the precipitable water vapor during this period was studied using all the water vapor sensors at Andros Island. The measurements revealed two drying episodes related to hurricane-induced midtropospheric subsidence. We believe these to be the first extended ground-based measurements of water vapor made in the near vicinity of a hurricane and a significant improvement over radiosonde measurements alone. Using the SRL profiling capability, the evolution of precipitable water was studied by layers, indicating that the predominant changes in column water occurred above 1 km. The layer between the surface and 1 km was representative of a well-mixed marine boundary layer with relatively constant mixing ratio throughout the layer. There also was evidence of midtropospheric humidification due to rainfall on August 24.

The evolution of cirrus cloud geometry and optical depth were studied as well. The influence of multiple scattering on the lidar measurements was studied. An iterative technique was presented which corrects for the influence of multiple scattering and allows cirrus cloud bulk extinction to backscatter ratio and particle radius to be determined. After converting the UV optical depths to IR optical depths based on a comparison of SRL optical depth and GOES brightness temperatures, the predictions of satellite brightness temperatures from a simple radiative transfer model were compared with actual GOES brightness temperatures. These predictions indicated that satellite radiances are noticeably affected for cirrus optical depths above ~ 0.005 .

The influence of cirrus on retrieved parameters from GOES

satellite measurements was also studied. Larger errors were induced in the retrieved precipitable water than in the retrieved skin temperatures. Undetected cirrus should present a consistent high bias in GOES satellite retrievals of TPW. Using the cirrus cloud detection criteria of the most recent ISCCP analysis indicates this bias is up to 20% over water and 40% over land. Errors such as these could influence hurricane model initialization since cirrus clouds are abundant in the vicinity of a hurricane. Furthermore, cloud climatology studies based on SAGE II observations [Wang *et al.*, 1996] have indicated frequencies of subvisual cirrus near the tropical tropopause of up to 70%. This implies that the influence of undetected cirrus on satellite retrievals could be quite significant in tropical regions.

An important conclusion of this effort is that satellite retrieval algorithms need to be able to detect the presence of cirrus clouds with IR optical depths as small as 0.005 in order to avoid significant influences on satellite radiances and thus potential errors in retrievals. This is an order of magnitude lower than the cirrus optical depth detection goal established in the EOS science plan [King, 1999]. Improved satellite measurement strategies such as the 1.375 μm cirrus channel of the MODIS instrument (<http://modarch.gsfc.nasa.gov/MODIS/>) on the recently launched and upcoming Terra and Aqua satellites are needed to improve satellite sensitivity to cirrus. However, the 1.375 μm channel is only effective at detecting cirrus during the daytime. Therefore studies similar to that performed here are needed to determine the effectiveness of cirrus detection from satellite during both the daytime and the nighttime to determine if there are diurnal biases in the IR satellite precipitable water record due to undetected cirrus.

Acknowledgments. The authors wish to acknowledge the important efforts of numerous individuals in this study: Bob Knutesen, Nick Bower, Paul van Delst, and Ken Vinson from the Space Science and Engineering Center of the University of Wisconsin for several sets of data, including the AERI-GOES retrievals, radiosonde, GPS, and standard meteorological data; Prentiss Moore and Don Penny of NASA GSFC Wallops Flight Facility for radiosonde data from Andros Island; Brent Holben and the NASA GSFC AERONET (Aerosol Robotic Network) effort for use of a Cimel Sun photometer and the processing of the data which are now part of the vast database of such measurements maintained at <http://aeronet.gsfc.nasa.gov:8080/>; Ping Yang for insightful discussions concerning cirrus particle phase functions; and all the individuals who helped to make the deployment of the SRL to Andros Island successful: Jeff Freemire, Fred Huegel, Gerry McIntire, Wallace McMillan, Steve Palm, Stacy Wise, Glenn Staley, and Dan Wooten. Finally, the authors would like to acknowledge the support of Ramesh Kakar, head of NASA's Atmospheric Dynamics and Remote Sensing Program, which made this experiment possible.

References

- Ansmann, A., U. Wandinger, M. Riebesell, C. Weitkamp, and W. Michaelis, Independent measurement of extinction and backscatter profiles in cirrus clouds by using a combined Raman elastic-backscatter lidar, *Appl. Opt.*, **31**(33), 7113–7131, 1992.
- Bohren, C. F., and D. R. Huffman, *Absorption and Scattering of Light by Small Particles*, 530 pp., John Wiley, New York, 1983.
- Beutler, G., I. I. Mueller, and R. E. Neilan, The International GPS Service for Geodynamics (IGS): Development and start of official service on January 1, 1994, *Bull. Geod.*, **68**, 1, 1994.
- Demoz, B. B., D. O'C. Starr, D. N. Whiteman, K. Evans, and D. Hlavka, Raman LIDAR detection of cloud base, *Geophys. Res. Lett.*, **27**(13), 1899–1902, 2000.
- DeSlover, D. H., W. L. Smith, P. K. Piironen, and E. W. Eloranta, A methodology for measuring cirrus cloud visible-to-infrared spectral optical depth ratios, *J. Atmos. Ocean. Technol.*, **16**, 251–262, 1999.
- Duan, J. M., et al., Remote Sensing Atmospheric Water Vapor using the Global Positioning System, *J. Appl. Meteorol.*, **35**, 830–838, 1996.
- Ellingson, R. G., and W. J. Wiscombe, The spectral radiance experiment (SPECTRE): Project description and sample results, *Bull. Am. Meteorol. Soc.*, **77**, 1967–1985, 1996.
- Elliott, W. P., R. J. Ross, and B. Schwartz, Effects on climate records of changes in National Weather Service humidity processing procedures, *J. Clim.*, **11**, 2424–2436, 1998.
- Eloranta, E. W., Practical model for the calculation of multiply scattered lidar returns, *Appl. Opt.*, **37**(12), 2464–2472, 1998.
- Eloranta, E. W., A high spectral resolution lidar for long-term unattended operation in the Arctic, in *Proceeding of the Tenth ARM Science Team Meeting*, Dep. of Energy, Washington, D. C., 2000.
- Eloranta, E. W., and P. Piironen, Measurements of particle size in cirrus clouds with the high spectral resolution lidar, paper presented at the Eighth International Workshop on Multiple Scattering Lidar Experiments, Def. Res. Estab. Valcentier, Courcellette, Quebec, Canada, 1996.
- Evans, K. D., S. H. Melfi, R. A. Ferrare, and D. N. Whiteman, Upper tropospheric temperature measurements with the use of a Raman lidar, *Appl. Opt.*, **36**, 2594–2602, 1997.
- Evans, K. D., B. B. Demoz, D. N. Whiteman, G. K. Schwemmer, W. Feltz, and D. Tobin, Laser remote sensing of the atmosphere, in *20th International Laser Radar Conference*, edited by A. Dabas and J. Pelon, Ecole Polytech., Paris, France, 2000.
- Feltz, W. F., W. L. Smith, R. O. Knuteson, H. E. Revercomb, H. M. Woolf, and H. B. Howell, Meteorological applications of temperature and water vapor retrievals from the ground-based atmospheric emitted radiance interferometer (AERI), *J. Appl. Meteorol.*, **37**, 857–875, 1998.
- Ferrare, R. A., S. H. Melfi, D. N. Whiteman, and K. D. Evans, Raman Lidar measurements of Pinatubo aerosols over southeastern Kansas during November–December 1991, *Geophys. Res. Lett.*, **19**, 1599–1602, 1992.
- Ferrare, R. A., S. H. Melfi, D. N. Whiteman, K. D. Evans, F. J. Schmidlin, and D. O'C. Starr, A comparison of water vapor measurements made by Raman lidar and radiosondes, *J. Atmos. Oceanic Technol.*, **12**, 1177–1195, 1995.
- Ferrare, R. A., S. H. Melfi, D. N. Whiteman, K. D. Evans, and R. Leifer, Raman lidar measurements of aerosol extinction and backscattering, 1, Methods and comparisons, *J. Geophys. Res.*, **103**, 19,663–19,672, 1998.
- Giver, L. P., C. C. Chackerian Jr., and P. Varanasi, Visible and near-infrared H₂¹⁶O line intensity corrections for Hitran-96, *J. Quant. Spectr. Radiat. Trans.*, **66**, 101–105, 2000.
- Grinfeld, T. C., and S. G. Warren, Representation of a nonspherical ice particle by a collection of independent sphere for scattering and absorption of radiation, *J. Geophys. Res.*, **104**, 31,697–31,709, 1999.
- Jackson, J. D., *Classical electrodynamics*, 2nd ed., 848 pp., John Wiley, New York, 1975.
- King, M. D., *EOS Science Plan—The State of Science in the EOS Program*, NASA publication http://eosps.gsfc.nasa.gov/sci_plan/chapters.html, 1999.
- Lesh, B. M., Reanalysis of radiosonde data from the 1996 and 1997 water vapor intensive operations periods: Applications of the Vaisala RS-80H contamination correction algorithm to dual-sonde soundings, in *Proceedings of the Ninth ARM Science Team Meeting*, Dep. of Energy, Washington, D. C., 1999.
- Melfi, S. H., D. N. Whiteman, and R. A. Ferrare, Observation of atmospheric fronts using Raman lidar moisture measurements, *J. Appl. Meteorol.*, **28**, 789–806, 1989.
- Melfi, S. H., K. D. Evans, J. Li, D. Whiteman, R. Ferrare, and G. Schwemmer, Observation of Raman scattering by cloud droplets in the atmosphere, *Appl. Opt.*, **36**(15), 3551–3559, 1997.
- Miller, E. R., J. Wang, and H. L. Cole, Correction for dry bias in Vaisala radiosonde RH data, in *Proceedings of the Ninth ARM Science Team Meeting*, San Antonio, TX, March 22–26, 1999, 1999.
- Prabhakara, C., R. S. Fraser, G. Dalu, M. C. Wu, and R. J. Curran, Thin cirrus clouds: Seasonal distribution over oceans deduced from Nimbus-4 IRIS, *J. Appl. Meteorol.*, **27**, 379–399, 1988.
- Ramamurthy, M. K., and B. F. Jewett, Ensemble prediction of Hurricane Opal's track and intensity, in *Proceedings of the AMS 23rd Conference on Hurricanes and Tropical Meteorology*, Boston, Mass., 1999.

- Reid, J. S., T. F. Eck, S. A. Christopher, P. V. Hobbs, and B. Holben, Use of the Angstrom exponent to estimate the variability of optical and physical properties of aging smoke particles in Brazil, *J. Geophys. Res.*, **104**, 27,473–27,489, 1999.
- Revercomb, H. E., W. F. Feltz, R. O. Knuteson, D. C. Tobin, P. F. W. van Delst, and B. A. Whitney, Accomplishments of the water vapor IOPs: An overview, in *Proceedings of the Eighth ARM Science Team Meeting*, Dep. of Energy, Washington, D. C., 1998.
- Rosow, W. B., and R. A. Schiffer, Advances in understanding clouds from ISCCP, *Bull. Am. Meteorol. Soc.*, **80**, 2261–2287, 2000.
- Sassen, K., and B. S. Cho, Subvisual-thin cirrus lidar data set for satellite validation and climatological research, *J. Appl. Meteorol.*, **31**(11), 1275–1285, 1992.
- Schmid, B., et al., Comparison of columnar water vapor measurements during the fall 1997 ARM Intensive Observation Period: Solar transmittance methods, *Appl. Opt.*, in press, 2000.
- Schmit, T. J., W. F. Feltz, W. P. Menzel, J. Jung, J. P. Nelson, and G. S. Wade, Validation and use of GOES sounder moisture information, *Bull. Am. Meteorol. Soc.*, in press, 2000.
- Sherlock, V., A. Hauchecorne, and J. Lenoble, Methodology for the independent calibration of Raman backscatter water-vapor lidar systems, *Appl. Opt.*, **38**, 5816–5837, 1999.
- Smith, W. L., S. Ackerman, H. Revercomb, H. Huang, D. H. DeSlover, W. Feltz, L. Gumley, and A. Collard, Infrared spectral absorption of nearly invisible cirrus clouds, *Geophys. Res. Lett.*, **25**, 1137–1140, 1998.
- Smith, W. L., W. E. Feltz, R. O. Knuteson, H. E. Revercomb, H. M. Woolf, and H. B. Howell, The retrieval of planetary boundary layer structure using ground-based infrared spectral radiance measurements, *J. Atmos. Oceanic Technol.*, **16**(3), 323–333, 1999.
- Suggs, R. J., G. J. Jedlovec, and A. R. Guillory, Retrieval of geophysical parameters from GOES: Evaluation of a split-window technique, *J. Appl. Meteorol.*, **37**, 1205–1227, 1998.
- Turner, D. D., W. F. Feltz, and R. A. Ferrare, Continuous water profiles from operational ground-based active and passive remote sensors, *Bull. Am. Soc.*, **81**, 1301–1317, 2000.
- Vaughan, G., D. P. Wareing, L. Thomas, and V. Mitev, Humidity measurements in the free troposphere using Raman backscatter, *Q. J. R. Meteorol. Soc.*, **114**, 1471–1484, 1988.
- Wade, C. G., An evaluation of problems affecting the measurement of low relative-humidity on the United States radiosonde, *J. Atmos. Oceanic Technol.*, **11**, 687–700, 1994.
- Wandinger, U., Multiple-scattering influence on extinction- and backscatter-coefficient measurements with Raman and high-spectral-resolution lidars, *Appl. Opt.*, **37**(3), 417–427, 1998.
- Wang, P.-H., P. Minnis, M. P. McCormick, G. S. Kent, and K. M. Skeens, A 6-year climatology of cloud occurrence frequency from Stratospheric Aerosol and Gas Experiment II observations (1985–1990), *J. Geophys. Res.*, **101**, 29,407–29,429, 1996.
- Warren, S. G., Optical constants of ice from the ultraviolet to the microwave, *Appl. Opt.*, **23**, 1206–1225, 1984.
- Whiteman, D. N., S. H. Melfi, and R. A. Ferrare, Raman lidar system for the measurement of water vapor and aerosols in the earth's atmosphere, *Appl. Opt.*, **31**(16), 3068–3082, 1992.
- Whiteman, D. N., and S. H. Melfi, Cloud liquid water, mean droplet radius, and number density measurements using a Raman lidar, *J. Geophys. Res.*, **104**, 31,411–31,419, 1999.
- Wolfe, D. E., and S. I. Gutman, Developing an operational, surface-based, GPS, water vapor observing system for NOAA: Network design and results, *J. Atmos. Oceanic Technol.*, **17**, 426–440, 2000.
- Wylie, D. P., and W. P. Menzel, Two years of cloud cover statistics using VAS, *J. Clim.*, **2**, 380–392, 1989.
- Wylie, D. P., and W. P. Menzel, Eight years of high cloud statistics using HIRS, *J. Clim.*, **12**, 170–184, 1999.
- Wylie, D. P., P. Piironen, W. Wolf, and E. Eloranta, Understanding satellite cirrus cloud climatologies with calibrated lidar optical depths, *J. Atmos. Sci.*, **52**(23), 4327–4343, 1995.
- Yang, P., K. N. Liou, and W. P. Arnott, Extinction efficiency and single-scattering albedo for laboratory and natural cirrus clouds, *J. Geophys. Res.*, **102**, 21,825–21,835, 1997.
- Yang, P., and K. N. Liou, Single-scattering properties of complex ice crystals in terrestrial atmosphere, *Contrib. Atmos. Phys.*, **71**(2), 223–248, 1998.

M. Cadirola, B. Demoz, K. D. Evans, S. H. Melfi: University of Maryland, Baltimore County, Catonsville, MD 21228.

W. Feltz and D. Tobin, Space Science and Engineering Center, University of Wisconsin, Madison, WI 53706.

S. I. Gutman, NOAA Forecast Systems Laboratory, Boulder, CO 80401.

G. J. Jedlovec, NASA Global Hydrology and Climate Center, Marshall Space Flight Center, Huntsville, AL 35811.

F. J. Schmidlin, G. K. Schwemmer, D. O'C. Starr, D. N. Whiteman, Earth Sciences Directorate Code 924, NASA, GSFC, Greenbelt, MD 20771. (david.whiteman@gsfc.nasa.gov)

(Received February 24, 2000; revised August 10, 2000; accepted August 16, 2000.)